

Influence of Irregular Coastlines on a Tornadoic Mesovortex in the Pearl River Delta during the Monsoon Season. Part I: Pre-storm Environment and Storm Evolution

Lanqiang BAI, Dan YAO, Zhiyong MENG, Yu ZHANG, Xianxiang HUANG, Zhaoming LI, Xiaoding YU

Citation: Bai, L. Q., D. Yao, Z. Y. Meng, Y. Zhang, X. X. Huang, Z. M. Li, and X. D. Yu 2024: Influence of Irregular Coastlines on a Tornadoic Mesovortex in the Pearl River Delta during the Monsoon Season. Part I: Pre-storm Environment and Storm Evolution, *Adv. Atmos. Sci.*, 41, 1115–1131. doi: [10.1007/s00376-023-3095-5](https://doi.org/10.1007/s00376-023-3095-5).

View online: <https://doi.org/10.1007/s00376-023-3095-5>

Related articles that may interest you

[Cloud Condensation Nuclei over the Bay of Bengal during the Indian Summer Monsoon](#)

Advances in Atmospheric Sciences. 2018, 35(2), 218 <https://doi.org/10.1007/s00376-017-6331-z>

[Aerosol Optical Properties and Radiative Impacts in the Pearl River Delta Region of China during the Dry Season](#)

Advances in Atmospheric Sciences. 2018, 35(2), 195 <https://doi.org/10.1007/s00376-017-7092-4>

[Microphysical Characteristics of Precipitation during Pre-monsoon, Monsoon, and Post-monsoon Periods over the South China Sea](#)

Advances in Atmospheric Sciences. 2019, 36(10), 1103 <https://doi.org/10.1007/s00376-019-8225-8>

[Interdecadal Variations of the South Asian Summer Monsoon Circulation Variability and the Associated Sea Surface Temperatures on Interannual Scales](#)

Advances in Atmospheric Sciences. 2017, 34(7), 816 <https://doi.org/10.1007/s00376-017-6246-8>

[Reduced Sensitivity of Tropical Cyclone Intensity and Size to Sea Surface Temperature in a Radiative-Convective Equilibrium Environment](#)

Advances in Atmospheric Sciences. 2018, 35(8), 981 <https://doi.org/10.1007/s00376-018-7277-5>

[Predictability of South China Sea Summer Monsoon Onset](#)

Advances in Atmospheric Sciences. 2019, 36(3), 253 <https://doi.org/10.1007/s00376-018-8100-z>



AAS Website



AAS Weibo



AAS WeChat

Follow AAS public account for more information

• Original Paper •

Influence of Irregular Coastlines on a Tornadic Mesovortex in the Pearl River Delta during the Monsoon Season. Part I: Pre-storm Environment and Storm Evolution

Lanqiang BAI¹, Dan YAO², Zhiyong MENG³, Yu ZHANG⁴, Xianxiang HUANG⁵,
Zhaoming LI⁵, and Xiaoding YU⁶

¹*Foshan Tornado Research Center, and China Meteorological Administration Tornado Key Laboratory, Guangdong Meteorological Service, and Southern Marine Science and Engineering Guangdong Laboratory (Zhuhai), Guangdong 528000, China*

²*Meteorological Observation Centre, CMA, Beijing 100081, China*

³*Department of Atmospheric and Oceanic Sciences, and China Meteorological Administration Tornado Key Laboratory, School of Physics, Peking University, Beijing 100871, China*

⁴*Guangzhou Meteorological Observatory, CMA, Guangdong 511430, China*

⁵*Foshan Tornado Research Center, and China Meteorological Administration Tornado Key Laboratory, CMA, Guangdong 528000, China*

⁶*China Meteorological Administration Training Center, CMA, Beijing 528000, China*

(Received 31 May 2023; revised 17 October 2023; accepted 10 November 2023)

ABSTRACT

The Pearl River Delta (PRD), a tornado hotspot, forms a distinct trumpet-shaped coastline that concaves toward the South China Sea. During the summer monsoon season, low-level southwesterlies over the PRD's sea surface tend to be turned toward the west coast, constituting a convergent wind field along with the landward-side southwesterlies, which influences regional convective weather. This two-part study explores the roles of this unique land–sea contrast of the trumpet-shaped coastline in the formation of a tornadic mesovortex within monsoonal flows in this region. Part I primarily presents observational analyses of pre-storm environments and storm evolutions. The rotating storm developed in a low-shear environment (not ideal for a supercell) under the interactions of three air masses under the influence of the land–sea contrast, monsoon, and storm cold outflows. This intersection zone (or “triple point”) is typically characterized by local enhancements of ambient vertical vorticity and convergence. Based on a rapid-scan X-band phased-array radar, finger-like echoes were recognized shortly after the gust front intruded on the triple point. Developed over the triple point, they rapidly wrapped up with a well-defined low-level mesovortex. It is thus presumed that the triple point may have played roles in the mesovortex genesis, which will be demonstrated in Part II with multiple sensitivity numerical simulations. The findings also suggest that when storms pass over the boundary intersection zone in the PRD, the expected possibility of a rotating storm occurring is relatively high, even in a low-shear environment. Improved knowledge of such environments provides additional guidance to assess the regional tornado risk.

Key words: tornado, mesovortex, surface boundary, land–sea contrast, monsoon

Citation: Bai, L. Q., D. Yao, Z. Y. Meng, Y. Zhang, X. X. Huang, Z. M. Li, and X. D. Yu, 2024: Influence of irregular coastlines on a tornadic mesovortex in the Pearl River Delta during the monsoon season. Part I: Pre-storm environment and storm evolution. *Adv. Atmos. Sci.*, **41**(6), 1115–1131, <https://doi.org/10.1007/s00376-023-3095-5>.

Article Highlights:

- A convergent boundary routinely forms on the west coast of the trumpet-shaped Pearl River Delta during the summer monsoon season.
- The tornadic mesovortex develops where storm-generated cold outflows intersect with the convergent boundary along the west coast.
- The triple point formed by three air masses in the influence of the unique land–sea contrast contributes to the rotating storm development.

* Corresponding authors: Lanqiang BAI, Dan YAO
Emails: bailanqiang@foxmail.com, yaod@cma.gov.cn

1. Introduction

While tornadoes have been reported on every continent except Antarctica, their occurrences show a distinct diversity worldwide. Most tornadoes are found in the United States. According to the tornado records during 2010–21 provided by the Storm Prediction Center, approximately 1200 tornadoes struck the United States each year. The regional climate has been demonstrated to be responsible for the large-scale environments that repeatedly favor tornadic storms in that region (Brooks et al., 2003). Owing to the unstable low-level air from the Gulf of Mexico, the large lapse rate in the central United States and the regularly large vertical wind shear in spring contribute to the high tornado occurrence (Markowski and Richardson, 2010).

Statistical studies have suggested that a broad spectrum of vertical wind shear and conditional instability combinations is capable of producing tornadoes. Significant severe thunderstorms that produce tornadoes are in general associated with high shear and high CAPE environments (Brooks et al., 2003). The ambient vertical wind shear is one of the important sources of low-level vertical vorticity within thunderstorms as a result of tilting and subsequent stretching of horizontal vorticity (Rotunno, 1981; Davies-Jones, 1984; Rotunno and Klemp, 1985). Supercellular tornadoes have been demonstrated to preferentially form in high-shear environments (Rotunno and Klemp, 1985; Thompson et al., 2013; Anderson-Frey et al., 2019).

In the high-shear region with large spatial coverage over the Great Plains, surface convergent boundaries such as drylines are often helpful to narrow the potential locations of severe thunderstorms and tornado development (Xue and Martin, 2006a, b; Weckwerth and Parsons, 2006). Some violent tornadoes are documented to have been spawned by supercells that initiate along drylines, such as the EF5 Moore tornado in 2013 (e.g., Atkins et al., 2014; Burgess et al., 2014; Zhang et al., 2015). Along the entire dryline length, typically hundreds of kilometers, the so-called “triple point” (Reed and Albright, 1997; Weiss and Bluestein, 2002; Wakimoto et al., 2006), where three different air masses intersect, is a common location for the initiation and intensification of tornadic supercells (e.g., the EF3 El Reno tornado; Wurman et al., 2014; Schumacher, 2015). The pre-existing enhanced vertical vorticity along boundaries or over the intersection zone by multiple boundaries could be a source of the initial vortex for stretching by large persistent and strong updrafts (e.g., Wakimoto and Wilson, 1989; Houston and Wilhelmson 2007a, b; Schenkman et al., 2012).

Although the pre-existing ambient vertical vorticity is typically an order of magnitude smaller than the horizontal vorticity that is ultimately tilted in the vertical direction, the pre-existing vertical vorticity seems to be important in the case of high-CAPE, low-shear tornadic events (Davies-Jones, 2006; Houston and Wilhelmson, 2012). More often, tornadoes that are associated with enhanced vertical vorticity

(e.g., misocyclones) along boundaries result from non-mesocyclone processes, which typically are more difficult to forecast (Brady and Szoke, 1989; Wakimoto and Wilson, 1989; Lee and Wilhelmson 1997a, b, 2000). Statistical analyses have suggested that storms in low-shear environments are often unfavorable for supercellular organization and sometimes are quasi-linear convective systems (QLCSs) and disorganized cells or clusters (Thompson et al., 2003, 2012). Within these QLCSs, tornadoes and damaging straight-line winds are found to be closely associated with the embedded low-level meso- γ -scale vortex (i.e., mesovortex; 2–20 km in diameter; Orlanski, 1975). These storms are characterized by a 0–6 km bulk wind shear magnitude of generally lower than 15 m s⁻¹ (Thompson et al., 2003). However, the presence of airmass boundaries may locally enhance the directional shear even in a large-scale low-shear environment, which sometimes alters the near-storm environment toward becoming more favorable for supercellular organization by a substantial increase in low-level shear.

In East Asia, eastern China is also characterized by climatologically tornado-favorable conditions (Brooks et al., 2003). However, according to a recently compiled reliable database during the time period of 2007–23, the tornado occurrences in China are only approximately 5% of those in the United States. The difference in regional climate results in the large discrepancy in tornado occurrences between the two countries (Zhou et al., 2022). As for the spatial distribution, tornadoes in China tend to be concentrated in coastal areas in eastern China, especially in the provinces of Guangdong and Jiangsu (Fan and Yu, 2015; Bai et al., 2020a). Compared to their midlatitude counterparts in the United States, tornadoes in Guangdong Province are located closer to the tropics (Fig. 1a). Tornadoes in this region are generally weak (Fan and Yu, 2015), which makes it even more challenging to detect and issue warnings. According to the statistics collected by the Foshan Tornado Research Center, the Pearl River Delta (PRD) has the highest tornado occurrences across Guangdong Province (Fig. 1a). The specific topography and regional climate in the PRD may have led to the relatively concentrated rather than random distribution.

The PRD coast is concave toward the sea, constituting a “trumpet” or “triangle” shape (Fig. 1b). After the onset of South China Sea summer monsoon, which typically occurs in late May over the South China Sea (Wang and LinHo, 2002), the prevailing low-level southwesterlies along with warm and moist air travel onshore (e.g., Du and Chen, 2019a; Bai et al., 2020b), which often repeatedly produce baroclinic boundaries near coasts due to the land–sea contrast. When storms take place in the PRD region, these boundaries may interact with the storm-generated outflows, forming new convergent boundaries. Compared to the relatively random locations of drylines in the Great Plains, the locations of convergent boundaries that are associated with land–sea contrast are seemingly relatively fixed in this region. For years, forecasters have supposed that the trumpet-shaped PRD coastline may play a role in the development of tornadic

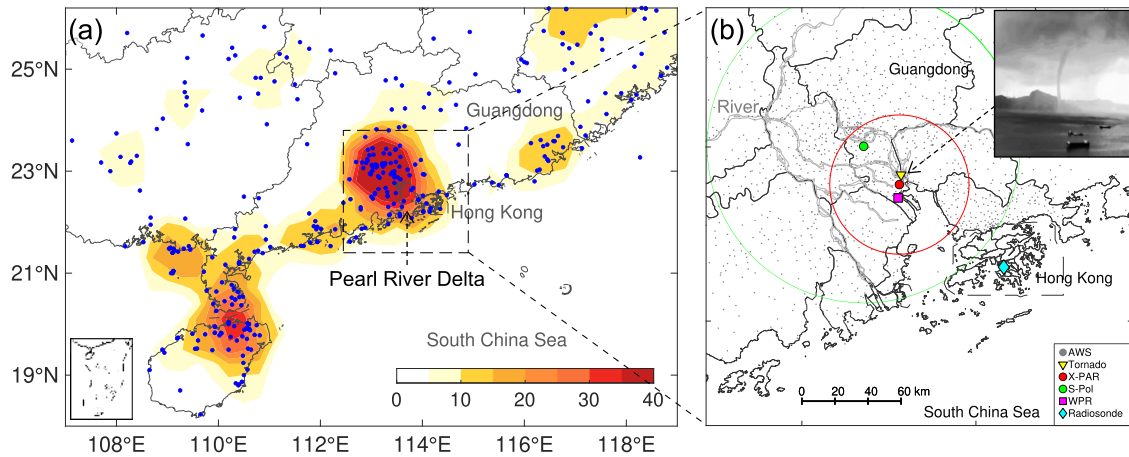


Fig. 1. (a) Tornado locations (blue dots) over the period from 2007 to 2022. The shading denotes the number of tornado occurrences within a range of 50 km. These tornado records were provided by Peking University (Zhou et al., 2022) and the Foshan Tornado Research Center. (b) Enlarged area of the dashed rectangle in (a), showing the observational platforms used for analysis in this study. The locations of the tornado (inset panel), X-PAR, S-Pol, the wind-profiling radar (WPR), radiosonde, and automatic weather station (AWS) are denoted by the triangle, red dot, green dot, square, diamond, and gray dot, respectively.

storms. The deployment of X-band phased array radars since 2018 in the PRD provides an opportunity to investigate in detail the formation process of tornadic storms with the aid of high spatiotemporal resolution sampling capacity. While the PRD is a climatological tornado hotspot in China, the annual number of tornado occurrences is still relatively low. More case studies are needed to better understand the formation and detection of tornadoes in this region.

The purpose of this two-part study is to explore the roles played by the trumpet-shaped coastline and its associated perturbed monsoonal flows in the formation of a tornadic storm in the PRD region. Part I primarily presents the mean state of the low-level atmosphere due to the land–sea contrast, the fine-scale evolution of the tornadic storm, and the pre-storm environments in the combined influence of the monsoon, land–sea contrast, storm outflows, and unique topography. Part II complements the observational analysis and explores the detailed dynamics of mesovortex formation via convection-permitting numerical simulations. This storm developed in a low-shear environment where commonly a non-mesocyclone process is expected. Tornadic storms that initiate in low-shear flows are typically more difficult to forecast than those in a high-shear environment. Understanding the formation processes of such tornadic storms may assist the refinement of methods used for tornado risk assessment in this region.

The remainder of this paper is organized as follows: Section 2 presents the mean state of the low-level atmosphere due to the land–sea contrast. The pre-storm environments of the tornadic storm are described in section 3. Section 4 gives an observational analysis of the storms, gust fronts, and surface flows. Sections 5 and 6 are the discussion and concluding remarks, respectively.

2. Coastal convergence associated with land–sea contrast

2.1. Design of numerical simulations

To obtain the mean state of the low-level atmosphere in the PRD region, a set of daily successive numerical simulations was conducted during three monsoon months using the Advanced Research version of the Weather Research and Forecasting (WRF) model (Skamarock et al., 2008), version 3.9.1. The WRF simulation was configured in one domain with a horizontal grid spacing of 4 km, covering the area shown in Fig. 1a. There were 50 terrain-following hydrostatic–pressure vertical levels topped at 50 hPa. The main parameterization configurations included the WSM6 microphysics scheme (Hong and Lim, 2006), the YSU boundary layer scheme (Noh et al., 2003), the revised MM5 Monin–Obukhov surface layer scheme, the thermal diffusion land surface scheme, the RRTM longwave radiation scheme (Mlawer et al., 1997), and the Dudhia shortwave radiation scheme. The cumulus parameterization scheme was turned off. The initial and lateral boundary conditions were provided by ERA5 gridded data (horizontal resolution: 0.25°; temporal resolution: hourly; Hersbach et al., 2020). The model was initialized at 0000 UTC for a 30-h simulation on each day during June from 2019 to 2021. The first 6 h was regarded as the model spin-up time, and thus the hourly output data for the last 24 h of the simulation were saved for analysis.

2.2. Mean state of the low-level atmosphere over the PRD during June

Figure 2 presents the mean state of the thermodynamic and kinematic characteristics of the near-ground atmosphere during June from 2019 to 2021. A distinct land–sea contrast in potential temperature at low levels was located over the

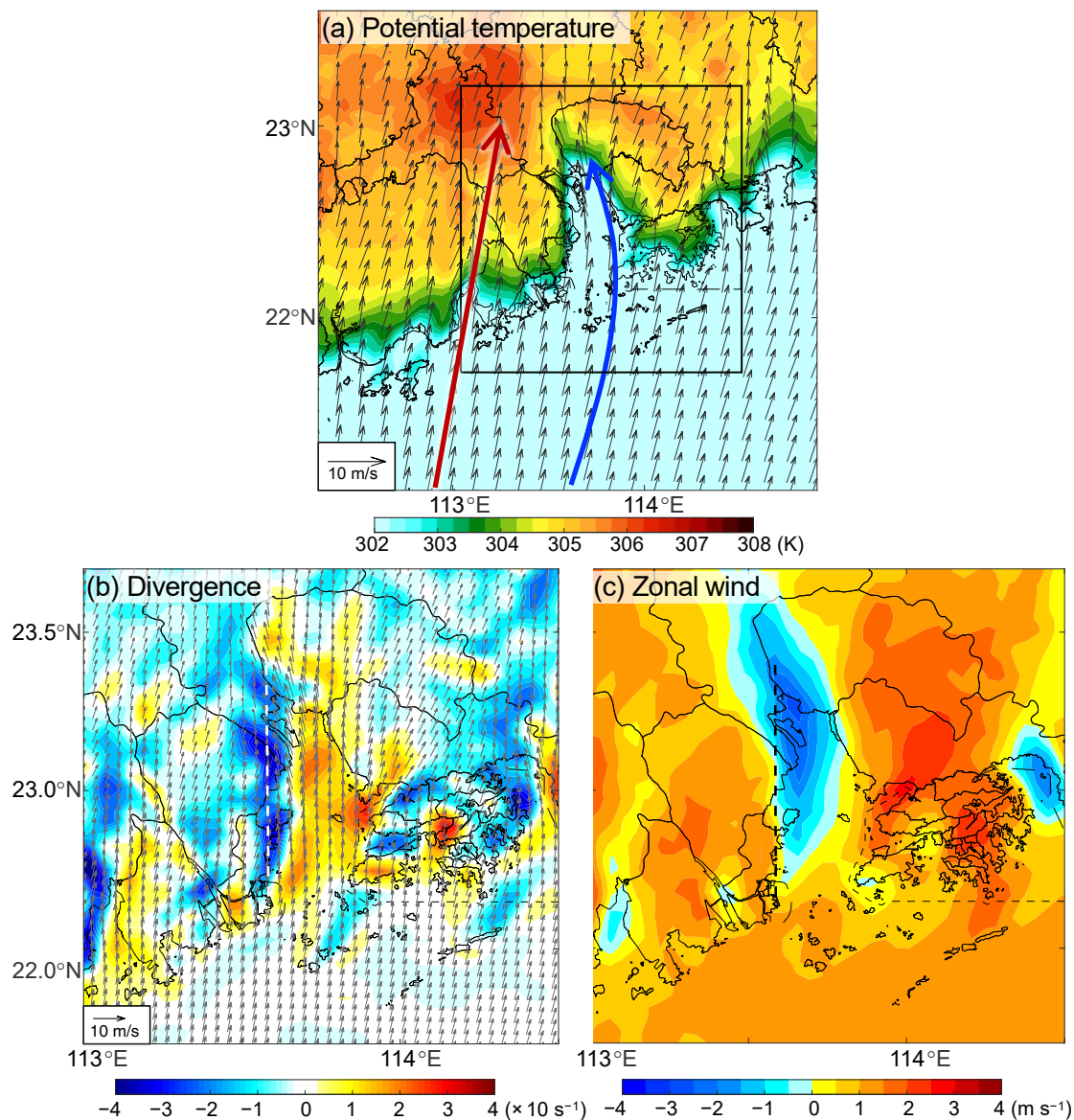


Fig. 2. (a) Average potential temperature (shaded) and horizontal winds (vectors) at 1500 LST in June from 2019 to 2021 obtained from the WRF simulations at the lowest model level. The red arrow represents the low-level prevailing onshore flows, and the blue curved arrow represents the sheared onshore flows due to the land–sea contrast. (b) As in (a) but for the average convergence (cool colors) and divergence (warm colors) enlarged in the rectangle in (a). (c) Average zonal components of horizontal winds at the lowest model level at 1500 LST (local standard time, LST = UTC + 8 h) in June from 2019 to 2021. The dashed lines denote the convergent boundaries along the west coast of the PRD.

PRD (Fig. 2a). In June, when the South China Sea summer monsoon becomes active, this region is typically characterized by southwesterly moist air flows traveling onshore at low levels. When these large-scale monsoonal flows arrive at the PRD coast, the prevailing low-level southwesterlies (red vector in Fig. 2a) tend to be horizontally sheared (blue vector in Fig. 2a), due to the land–sea contrast.

In the presence of the land–sea contrast of the trumpet-shaped coastline, the downward branch of the sea breeze circulation over the PRD sea surface contributes to a tendency of the easterly wind component on the west coast. On the

other hand, greater friction force is expected between the underlying surface and the bottom of the atmosphere on the landward side. In the afternoon, the heated land strengthens the turbulent exchanges of momentum and thus also decelerates the lower-troposphere onshore flows on the coastal land. Consequently, a negative tendency of the u component of the near-surface flow is expected in the west coastal area (Figs. 2b, c). The sheared onshore flows over the PRD sea surface thus routinely produce a low-level convergence zone (dashed lines in Figs. 2b, c) along the west PRD coast, and a divergence zone over the sea surface. In comparison to the rel-

actively random locations of drylines in the Great Plains, this convergent boundary (ellipse in Fig. 2b) appears to be topographically locked.

The fundamental fact is that the topography is fixed and the summer monsoon occurs every year, indicative of a connection between the frequently occurring local severe weather and the unique topography and regional climate. Considering the relatively high frequency of tornado occurrence over the PRD region, the current study attempts to investigate the role of such an airmass boundary that is associated with the land–sea contrast in the regional tornadic storms. To reach that point, the first part of this study involves a detailed observational analysis of a tornadic storm in this area. The tornadic case occurred during the active monsoon season in 2020 when multiple X-band phased-array weather radars were deployed and were operating in real time, which provided an opportunity to analyze the fine-scale storm structures at high temporal resolution.

3. Pre-storm environment of the tornadic storm

3.1. Observational and model data

For the purposes of synoptic and mesoscale analysis, observational data from surface weather stations, radiosondes, and ERA5 reanalysis gridded data were used. The densely deployed surface weather stations (gray dots in Fig. 1b) provide surface observations at an interval of 5 min. The nearby radiosonde (rhombus in Fig. 1b) and a wind profiling radar (square in Fig. 1b) were employed to obtain vertical profiles, including air temperature, moisture, and horizontal winds. The radiosonde was routinely launched twice a day and the profiles from the wind profiling radar were available every 6 min with a vertical resolution of 100 m.

Two operational weather radars were used to depict the storm evolutions, including an S-band China New Generation Doppler Weather Radar with dual-polarization capability (S-pol; green dot in Fig. 1b) and an X-band dual-polarization phased-array weather radar (X-PAR; red dot in Fig. 1b). The S-pol operated in the volume coverage pattern 21 (VCP21) mode during this event with a volumetric update time of approximately 6 min and a radial gate spacing of 250 m. The X-PAR was located approximately 6 km to the south of the reported tornado and operated an electronically scanned X-band planar antenna with dual polarization. The 360° volumetric update time was 90 s with 12 elevation angles (0.9°, 2.7°, 4.5°, 6.3°, 8.1°, 9.9°, 11.7°, 13.5°, 15.3°, 17.1°, 18.9° and 20.7°). The radial gate spacing was 30 m. By adopting the oversampling technique, the azimuthal interval was 0.9°.

3.2. Synoptic and mesoscale atmospheric conditions

The tornadic storm of interest occurred in the early afternoon on 1 June 2020, after the onset of the summer monsoon. It spawned a short-lived tornado (~7 min) at approxi-

mately 1250 LST (local standard time, LST = UTC + 8 h) over the Pearl River estuary (Fig. 1b; Zhang et al., 2021). The lower troposphere was characterized by prevailing monsoonal southwesterlies in the coastal region of South China in the early morning, as indicated by upper-air observations (Figs. 3a, b). A salient wind-shift line formed as the monsoonal southwesterlies converged with the subtropical westerlies (dashed curves in Fig. 3b). This synoptic forcing was responsible for the upstream mesoscale convective systems (MCSs) that were located to the west of Guangdong Province (labeled MCS-A in Fig. 4a). To the south of the wind-shift line, an 850-hPa jet stream was situated over the coastal land, leading to divergence at this level (dashed isopleth of 12 m s^{-1} in Fig. 3b). Such divergence combined with the near-surface convergence due to the sea–land transition would produce a favorable dynamic structure for low-level upward motion and thus the formation of coastal storms (Du and Chen, 2019b).

At 1130 LST, the PRD region was characterized by onshore southerlies near the surface (Fig. 3c). Under the influence of warm and humid tropical marine airmass advection, the region of interest had high thermodynamic instability with little convective inhibition. As revealed by the measurements of a Hong Kong sounding taken in the early morning, the calculated surface-based CAPE (with virtual temperature correction), LCL and LFC were 3447 J kg^{-1} , 361 m and 554 m, respectively (Fig. 5a). These high-CAPE and low-LCL values are known to be conducive to the development of vigorous moist convection. Although the thermodynamic conditions were favorable for the formation of deep moist convection, the dynamic variables were generally not supportive of supercellular organization. Figure 5 shows that the horizontal wind speeds were generally light in the whole column of the troposphere. The 0–6 km bulk wind difference was only 7.2 m s^{-1} , which is small for supercellular organization (Markowski and Richardson, 2010). The 0–1 km storm relative helicity (SRH) was only $42 \text{ m}^2 \text{ s}^{-2}$, which was calculated using the estimated storm-motion vector based on the method of Bunkers et al. (2000) for right-moving supercells. As shown in the hodograph diagram, the estimated storm motion (296° , 8.1 m s^{-1}) was toward the southeast (magenta vector in Fig. 5b). By tracking the radar echoes, the realistic storm motion (228° , 10.0 m s^{-1}) was toward a different direction (red vector in Fig. 5b). Using the realistic storm motion, the updated 0–1 km SRH value was reduced to only $7 \text{ m}^2 \text{ s}^{-2}$, suggesting a low potential for a cyclonic rotating updraft in right-moving supercells. Although dominated by unstable air masses prior to the tornadogenesis, the region of interest was characterized by marginal values of supercell composite parameter and significant tornado parameter (STP), due to the small SRH and bulk Richardson number shear (Thompson et al., 2003).

Figure 6 presents the evolution of wind profiles under the precipitation-free conditions obtained from the wind-profiling radar located approximately 15 km to the south of the tornado location (Fig. 1b). Consistent with the earlier sounding observations, the wind profiles derived from the wind-pro-

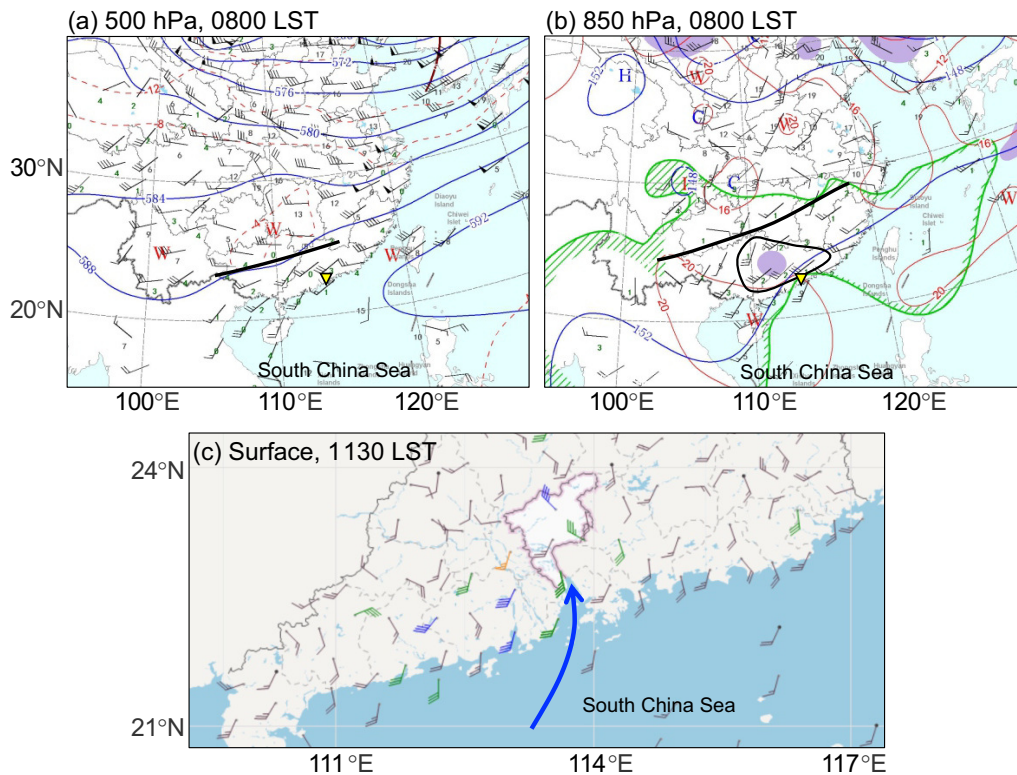


Fig. 3. Observed synoptic analysis at (a) 500 hPa, (b) 850 hPa, and (c) surface level on 1 June 2020. The background weather maps in (a, b) and (c) were originally produced by the National Meteorological Center and Guangzhou Meteorological Observatory, respectively. The tornado's location is marked by the yellow triangle. The half barbs, full barbs, and pennants denote 2, 4, and 20 m s^{-1} , respectively. In (a), geopotential height (units: dagpm), temperature (units: $^{\circ}\text{C}$), and the wind shift line are represented by blue, red, and dashed black curves, respectively. In (b), the dashed isopleth represents the area with a wind speed greater than 12 m s^{-1} at 850 hPa. The green isopleths mark the boundaries with a mixing ratio of 12 and 15 g kg^{-1} , respectively. The moist side is rasterized.

filing radar suggested that the lowest 500 m layer was generally characterized by southerlies and the upper layer by southwesterlies. Approximately one hour before tornadogenesis, the 1.5–2 km AGL layer underwent an enhancement of wind speed. The wind directions from the near-surface to 2 km AGL became more veering with height. Although the directional and speed shears between surface and upper layers increased before tornadogenesis, the integrated index of 0–1 km SRH was overall small, with a value generally less than $20 \text{ m}^2 \text{ s}^{-2}$. On the other hand, the speed enhancement near the top of the PBL may have enhanced the vertical momentum transport at lower levels, priming the mesoscale environment for convective initiation and development.

The above analyses suggest that the tornadic storm formed in the destabilized atmosphere ahead of a synoptic wind-shift line but in a low-shear environment. Although the high conditional instability supports convective development, the dynamic conditions suggest that this environment was marginally favorable for the expected supercellular storm type as indicated by the low values of vertical wind shear. The marginal STP values also suggest a very low potential for a supercellular tornado in the region of interest.

4. Observational analysis of the storms, gust fronts and monsoonal flows

4.1. Storm evolutions obtained from radar observations

The tornadic storm was embedded in the southern-end part of a QLCS (Fig. 4b). It initiated at approximately 1218 LST (Storm S2 in Fig. 7b) as part of multiple scattered convective cells that were aligned in a southwest–northeast orientation (the rectangle in Fig. 7a). The storm propagated toward the northeast and its northern part merged with a pre-existing storm (Storm S3) at 1236 LST (Fig. 7c). During the period from 1248 to 1254 LST, a southern storm (labeled S1) caught up and merged with the southern part of tornadic Storm S2 (Figs. 7d, e). A “hook” echo signature was identified between Storms S1 and S2 at the lowest radar level at 1254 LST (refer to the notch of reflectivity labeled Hook in Fig. 4b). The reported tornado was located slightly to the south of this hook echo. The subsequent X-PAR analysis in the following subsection provides more details on the fine-scale storm structures.

In the S-Pol volume scan when the tornadic storm initiated, a radar fine line was identified at the 0.5° elevation

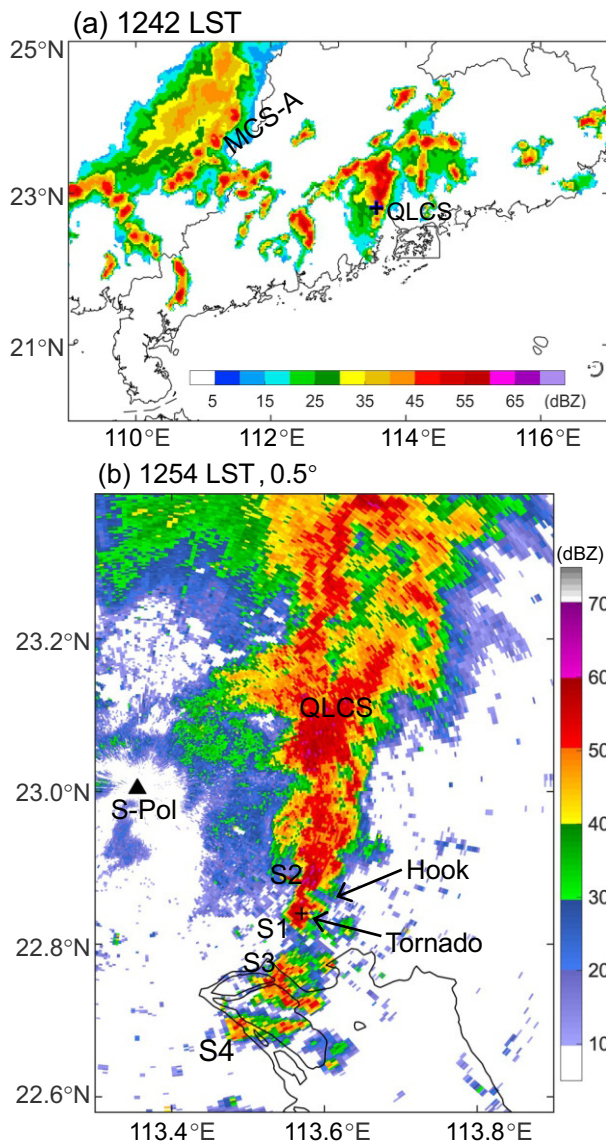


Fig. 4. (a) Composite radar reflectivity at 1242 LST 1 June 2020. (b) Radar reflectivity at the 0.5° elevation angle from S-pol at 1254 LST on 1 June 2020. The black cross marks the approximate tornado location.

angle (Fig. 7f). It was located approximately 7 km to the west of Storm S2. The surface observations from two surface weather stations (labeled A and B in Fig. 7f) confirmed that this radar fine line was the leading edge of storm cold outflows (i.e., gust front). These two stations were almost located on the radar fine line at 1218 LST. At Station A, a sharp decrease in surface temperature (4°C) and a slight pressure jump were observed from 1220 to 1225 LST (Fig. 8a). Meanwhile, the surface winds turned westerly from southwesterly and intensified to 15.1 m s⁻¹ from 8.2 m s⁻¹. The relative humidity also underwent an evident increase from 72% to 85% within 10 min. To the south of this station, Station B observed rapid changes in surface temperature, wind, humidity, and pressure from approximately 1215 LST (Fig. 8b). The confirmed gust front moved eastward and caught up with the tornadic storm at 1236 LST when this storm

merged with its northern Storm S3 (Fig. 7c).

The merging process was more clearly observed by X-PAR at a finer spatiotemporal resolution (Fig. 9). Prior to the hook echoes, a “finger-like” echo signature started to be identified by X-PAR from 1235:30 LST, and this signature was even more pronounced after 1240:00 LST. Note that the S-Pol observations suggest that the contact between the aforementioned gust front and the tornadic Storm S2 occurred nearly at that time (Fig. 7c), while the precise location of the gust front is difficult to confirm because of the interference of precipitation echoes. The station surface winds valid at 1235 LST indeed suggest that the gust front was in proximity to the tornadic storm at that time. The X-PAR radial velocity at the lowest radar level shows that the southwestern edge of Storm S2 underwent a transition from outbound to inbound radial velocity from 1231:00 to 1235:30 LST (Fig. 10). As shown in Fig. 10a, the distance between Station A and the western edge of Storm S2 was approximately 9 km and thus the average translation speed of the radar fine line was simply estimated as 8.8 m s⁻¹ during 1218–1235 LST. At Station C (Fig. 10a), during the passage of surface cold outflows, the observed wind speed was 9.6 m s⁻¹ at 1235 LST. Considering the deformation of the density current, it seems reasonable to presume that the gust front had almost interacted with Storm S2 at 1235 LST, after which the finger-like echo signature developed.

From 1245:00 to 1249:30 LST, there was an indication of reflectivity wrap-up, indicative of strong midlevel cyclonic rotations (Figs. 9c, d). At the 8.1° elevation angle, a well-defined meso- γ -scale cyclonic signature was identified near the tip of the finger-like echoes (Figs. 9e, f). While the radar-based structures of the tornadic storm present a supercellular organization, the storm is believed to be a non-mesocyclone process because closer inspection shows that the mesocyclonic rotation originated from low levels and was shallow in depth. Here, the meso- γ -scale cyclonic signature in the Doppler products represents a mesovortex. The mesovortex formed before the merger of Storms S1 and S2 (Figs. 9c–f). The maximum height of the measurable mesocyclonic signatures in all volume scans was approximately 4 km AGL. The distance of the maxima of the couplet signature in the radial velocity field ranged from 2 to 3 km (e.g., Fig. 9f and Fig. 11). In this study, the detailed quantitative evolution of the mesovortex structure is not presented because the velocity couplet features were sometimes incomplete due to the relatively low detection sensitivity of X-PAR. For example, the maxima in the outbound part of the velocity couplet signature in Fig. 9e was not measurable. Compared to typical supercells in the U.S. Great Plains, the current supercell-like storm was miniature. The fine structure of this hook echo signature was difficult to identify by the operational S-Pol radar (e.g., Fig. 4b).

Beneath the mesovortex, a weak tornadic vortex signature (TVS) was identified at the 0.9° elevation angle at 1251:00 LST when the northern part of Storm S1 had started to merge with the hook echoes of Storm S2 (Figs. 12a, b). Meanwhile, a relatively weak-echo “hole” signature was

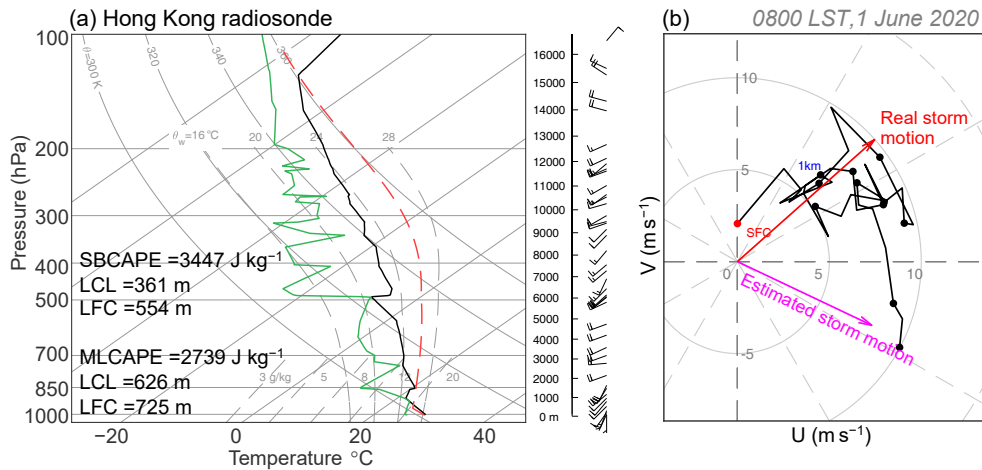


Fig. 5. (a) Skew- T log- p diagram showing the Hong Kong sounding launched at 0800 LST 1 June 2020. The ambient and dewpoint temperatures are represented by the solid black and green lines, respectively. The parcel that ascends undiluted from the surface is indicated by the dashed red curve (without virtual temperature correction). The half bars and full bars represent 2 and 4 m s^{-1} , respectively. (b) Hodograph plotted from the horizontal winds in (a). The red and magenta arrows represent the observed and computed storm motion [using the method proposed by Bunkers (2000)], respectively. The surface level is denoted by the red dot.

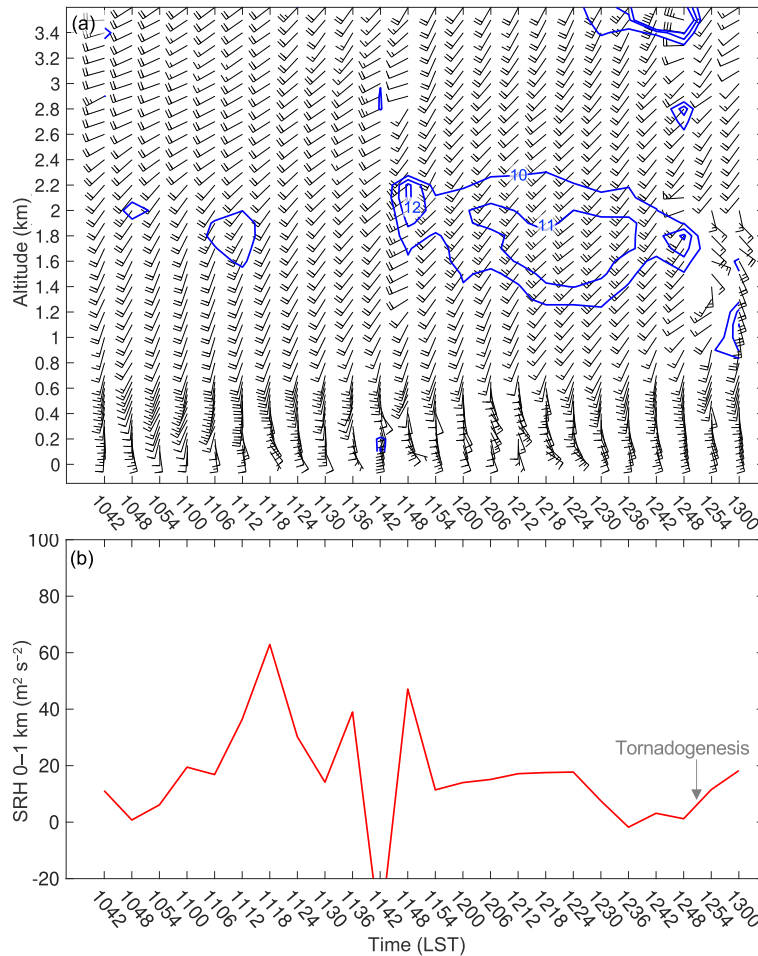


Fig. 6. (a) Horizontal winds (barbs) observed by the wind-profiling radar as described in Fig. 1b. The wind speeds are contoured in blue from 10 m s^{-1} . (b) The 0–1 km SRH calculated using the wind profiles in (a) from 1042 to 1300 LST 1 June 2020. The observed storm motion is used to calculate the SRH value.

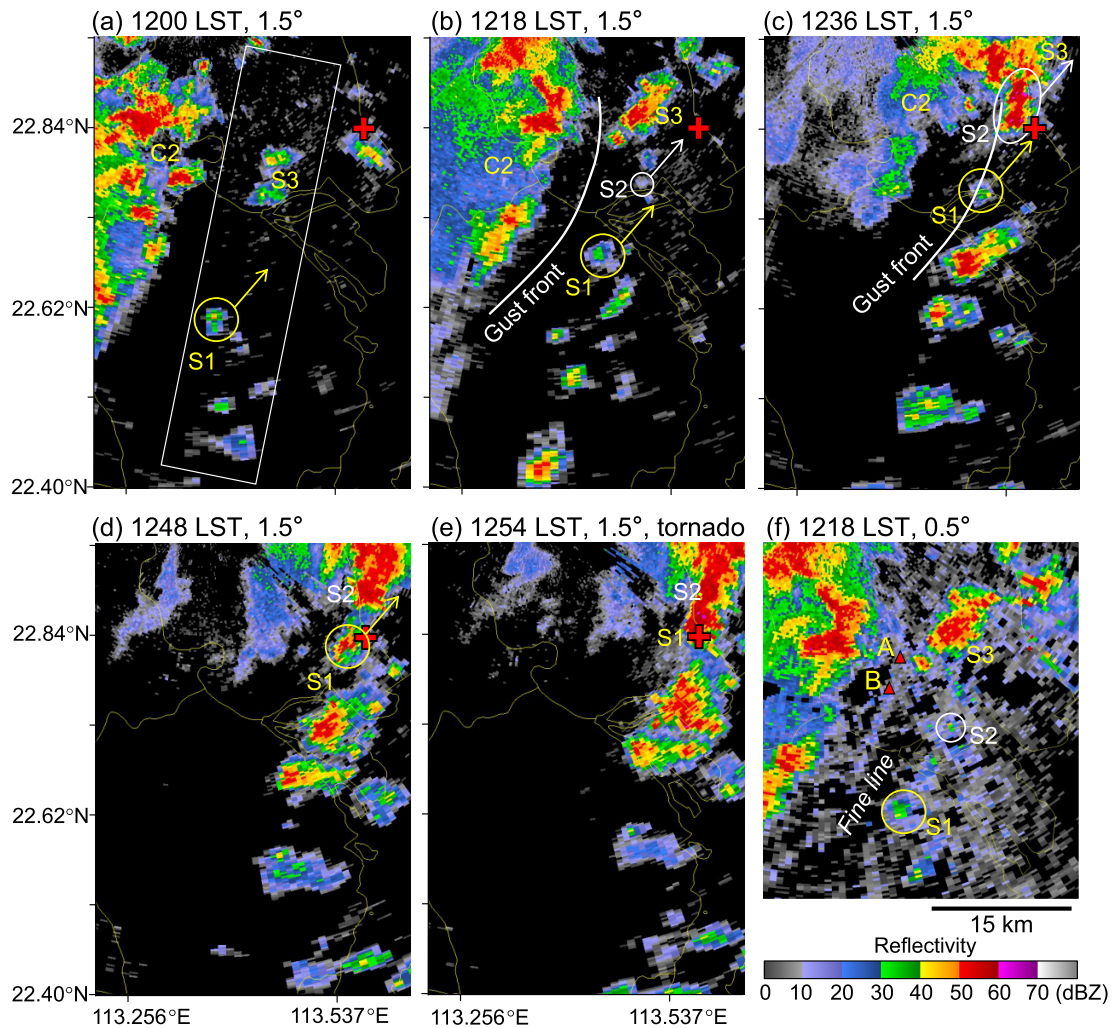


Fig. 7. Radar reflectivity at different elevation angles from S-pol as described in Fig. 1b. The red cross marks the approximate location of the tornado. The arrows represent the moving directions of the circled storms. The white curve in (b) marks the location of the gust front identified based on the fine line of reflectivity at the lowest radar level, as shown in (f). The hook echo region at the 0.5° elevation angle at 1254 LST is enlarged in (g). Triangles A and B shown in (f) represent the locations of the surface weather stations used in Fig. 8.

identified around the TVS (Figs. 12a–d). In the fields of the co-polar cross-correlation coefficient (ρ_{HV}) products, a localized area of small-value ρ_{HV} was identified near the TVS (inset in Fig. 12b). Low ρ_{HV} is often associated with lofted tornadic debris, which typically has random orientations and irregular shapes and thus results in a low ρ_{HV} signature. In the following volume scan, the maximum gate-to-gate radial velocity difference of the 0.9° TVS was 19 m s⁻¹, with anomalously low ρ_{HV} less than 0.6 (Fig. 12f). During the tornadic event, the diameter of the low- ρ_{HV} area was generally less than 400 m (insets in Figs. 12e–h). The TVS intensity peaked at 1254:00 LST, with a maximum gate-to-gate radial velocity difference of 22 m s⁻¹ at 420 m AGL (Fig. 12g). The TVS lost its clear identification after 1257:00 LST. The reflectivity fields from X-PAR also demonstrate that the tornado formed at the tip of the hook echo (Figs. 12a–d). Compared to the S-Pol observations (Fig. 4b), Fig.

12c shows two notches along the hook echo due to the merging process.

4.2. Collocation between the storm, gust front, and monsoonal flows

The aforementioned radar and surface observations provide evidence of the juxtaposition of finger-like echoes and the surface triple point. Figure 9a shows that before the formation of finger-like echoes, the southern part of Storm S2 was located at the triple point formed by the eastward-moving outflows and southwesterly and southeasterly flows (black, red and magenta curved arrows, respectively). After the gust front arriving at the triple point at approximately 1236 LST, the finger-like echoes developed and subsequently produced a low-level mesovortex in the following 5 min (e.g., Figs. 9b, e). The close proximity in time and space of the mesovortex to the surface triple point might have contributed to the gener-

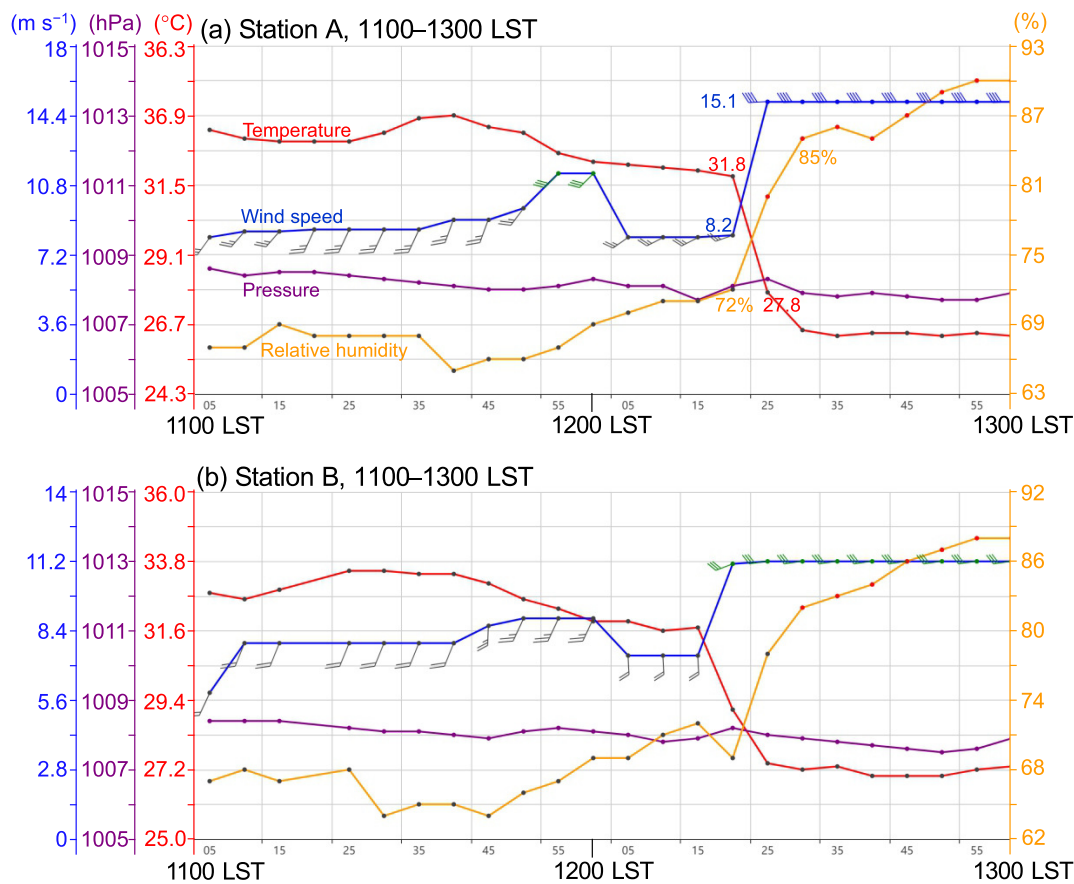


Fig. 8. Time series of surface temperature (red), wind speed (blue), pressure (purple), and relative humidity (orange) on 1 June 2020 obtained from surface weather stations A and B, as shown in Fig. 7f. The half barbs and full barbs represent 2 and 4 $m s^{-1}$, respectively.

ation of the mesovortex. Previous studies have suggested that enhanced low-level vertical vorticity along convergent boundaries sometimes directly promotes the formation of a mesocyclone or mesovortex and that longer-lived, strong low-level updrafts at these boundaries are more likely to support midlevel rotations (e.g., Houston and Wilhelmson, 2007b). The current analysis based on surface weather stations suggests that the triple point where three different air masses intersect was a source of pre-existing ambient vertical vorticity at low levels. The subsequent forced lifting associated with the gust front would further enhance the upward motions over the triple-point zone and thus intensify the stretching of the locally enhanced low-level vertical vorticity in that region. Based on the observational evidence, the fact is that the finger-like echoes and subsequent mesovortex formed when the gust front was intruding into the triple point zone. By conducting multiple sensitivity numerical simulations in Part II of this study, it is demonstrated that the triple point due to the trumpet-shaped coastline (through a sensitivity experiment that modifies the coastline shape) and the intruding gust front (through a sensitivity experiment that strengthens the cold pools) both played an important role in the formation of low-level mesovortex in this case.

In addition to the potentially important roles of the triple point and gust front in the mesovortex generation, it is

still not clear whether the merger between Storm S1 and the tornadic storm S2 (Figs. 9c, d) contributed to the intensification of the existing mesovortex (Fig. 11). Flounoy et al. (2022) documented that storm merging processes are quite common in supercell events. Although no general relationship has been found between storm merger and temporal changes in low-level mesocyclone strengths, qualitative results yield after thresholding the outcome of merger events on the mesocyclone strength before merger. Their statistics suggest that the initially weak mesocyclones are more likely to intensify after storm mergers, while the initially strong mesocyclones are more likely to weaken. In the current case, the weak mesovortex formed before the merger between Storm S1 and the hook echoes (e.g., Figs. 11d–f). It is a fact that the mesovortex intensified and then produced a tornado shortly after the merger event (Figs. 9 and 12). Although it is hard to demonstrate the exact role of the merger process in the mesovortex intensification and tornado-genesis, the cold pool outflows emanated from the approaching Storm S1 could have locally altered the near-storm-scale environments around the low-level mesovortex. During this case, multiple merger events occurred in the southern-end part of the QLCS. After the demise of the short-lived tornado, two storms (labeled S3 and S4 in Fig. 4b) to the south of the hook echoes caught up and merged with the hook

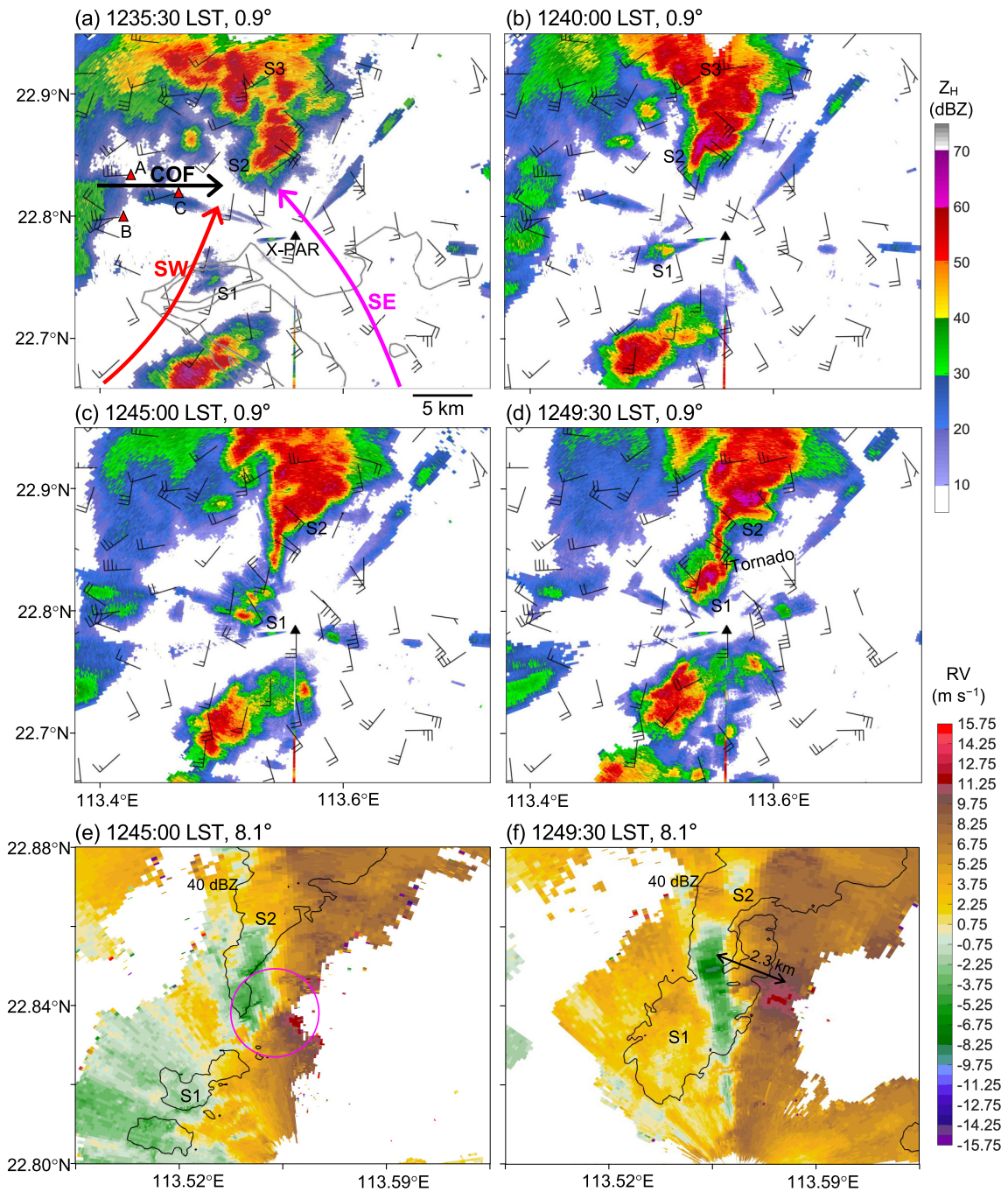


Fig. 9. (a–d) Reflectivity at the 0.9° elevation angle from X-PAR (black triangle) as described in Fig. 1b. The overlaid surface winds (barbs) are valid at (a) 1235, (b) 1240, (c) 1245, and (d) 1250 LST on 1 June 2020. The half barbs and full barbs represent 2 and 4 m s⁻¹, respectively. The black cross in (d) denotes the tornado’s location. (e, f) Radial velocity at the 8.1° elevation angle from X-PAR, showing the mesocyclone signature (magenta circle) near the hook echo. The black, red, and magenta arrows in (a) represent the direction of cold outflows (GF), southwesterly monsoonal flows (SW), and southeasterly monsoonal flows (SE), respectively, as described in the text. Surface weather stations marked by red triangles are labeled A, B and C.

echoes. Over the triple point, another supercell-like structure (labeled Hook echo B in Figs. 13a, b) in the rain field formed in the southern-end part of Storm S4. The radial velocity fields showed a mesocyclonic signature at the low radar levels but this meso- γ -scale vortex was overall weak and short-lived (Figs. 13c, d).

5. Discussion

During the active season of the South China Sea summer monsoon, the PRD area is significantly influenced by onshore southwesterlies in the lower troposphere. The onshore monsoonal flows present a salient feature of hori-

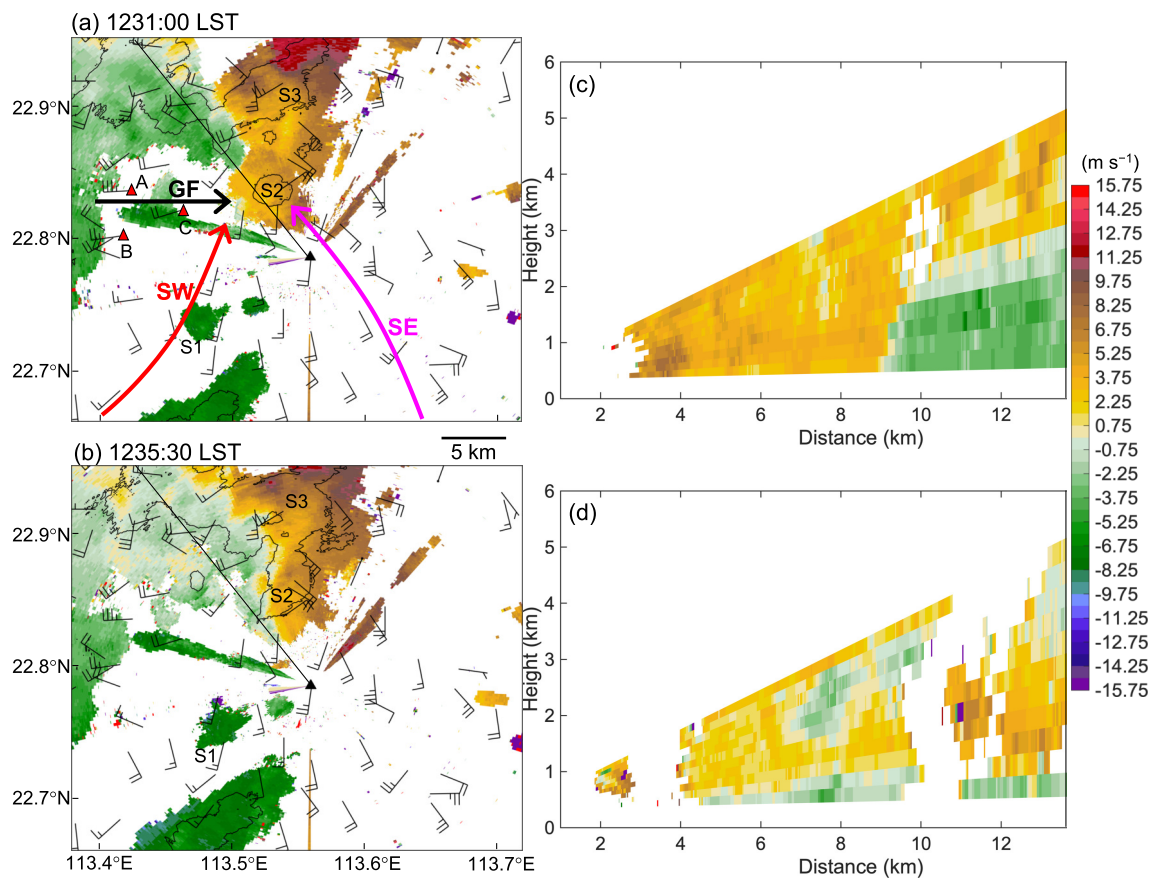


Fig. 10. (a, b) Radial velocity at the 0.9° elevation angle from X-PAR (black triangle) as described in Fig. 1b. The overlaid surface winds (barbs) are valid at (a) 1230 and (b) 1235 LST 1 June 2020. The half barbs and full barbs represent 2 and 4 m s^{-1} , respectively. The 40-dBZ reflectivity is contoured in black. The arrows and red triangles are the same as those in Fig. 9a. (c, d) Vertical cross-sections of radial velocity along the black lines in (a) and (d), respectively.

zonal heterogeneity over the estuary of the Pearl River due to the land–sea contrast of the trumpet-shaped coastline (Fig. 14a). This unique land–sea contrast leads to a routinely formed convergent boundary on the west coast under the influence of the warm southwesterlies on land and the sheared monsoonal flows with relatively cool air masses from the PRD sea surface. Chen et al. (2016) produced a radar climatology and carried out a set of sensitivity numerical simulations to investigate the characteristics of land–sea breezes and the related rainfall in this region. Their results suggested that convective rainfall is primarily located over the west coast of the PRD. After removing the inhomogeneity of the coastline (i.e., no trumpet shape), the semi-idealized numerical simulations showed a significantly different regional pattern of coastal convection in this area. These findings support the potential influence of the convergent boundary due to the trumpet-shaped coastline on the region’s convective weather.

When cold pools emanated from the northern storms block the onshore flows, three airmass boundaries are present, producing a triple point near the Pearl River estuary, as in this case (Fig. 14). The local maxima of vertical vorticity (e.g., misocyclones) along convergent boundaries that

originate from horizontal shearing instability (Kingsmill, 1995) increase the risks of rotating storms even under the dynamic conditions that are unfavorable for supercellular organization. In contrast with the along-boundary heterogeneity, the triple point caused by boundary intersections is also believed to create risk for an upcoming storm to organize into a rotating storm because of the pre-existing vertical vorticity in that region. Such a possibility would be even higher when storms successively propagate toward and pass over a triple point. On the other hand, because the position of the triple point is relatively slow-moving or fixed, a subsequent mismatch regarding the position between the triple point and mesovortex that propagates along with storms tends to be unfavorable for a strong midlevel rotation.

It should be noted that the PRD is a hotspot for thunderstorms (Zhang et al., 2017; Bai et al., 2020b), while tornadic storms are still rare events over the estuary of the Pearl River where the triple point often forms. This suggests that, even though the unique topography provides favorable conditions for a higher probability of rotating storms compared to the neighboring coasts of southern China, smaller storm-scale processes beyond the mesoscale environment may eventually determine the tornadogenesis. On the other hand, it is

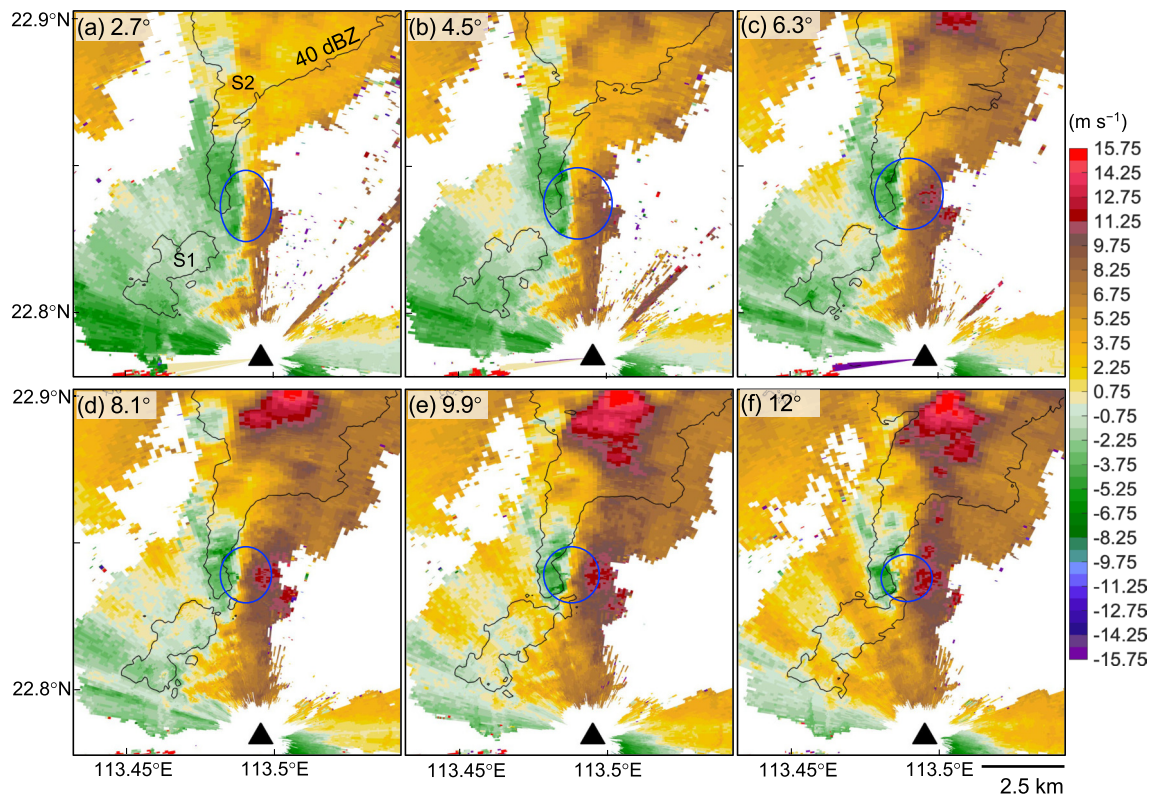


Fig. 11. Radial velocity at different elevation angles from X-PAR (black triangle) at 1246:30 LST 1 June 2020. The 40-dBZ reflectivity is contoured in black. The mesovortex signatures are manually marked by blue ellipses.

difficult to detect the vertically oriented vortices and estimate their strengths by Doppler weather radars. Previous studies have documented that some radars that incorporate high-power transmitters have the capability to detect mesocyclones (with weak ambient vertical vorticity) aligned with airmass boundaries, such as the mobile Doppler radars used during the International H₂O Project (Wurman et al., 1997; Marquis et al., 2007). In the last two years, dozens of polarimetric X-PARs have been deployed in the PRD region, but they are characterized by relatively low detection sensitivity due to their limited peak transmission power (~400 W), which makes it hard to detect these vortices in precipitation-free conditions. Nonetheless, owing to the dense deployment of surface weather stations in this region, a qualitative recognition could be achieved based on the horizontal winds measured by these stations. A combination of surface observations and the storm evolutions from radar products may still provide guidance for assessing severe weather over the triple-point zone.

6. Concluding remarks

In this paper, the pre-storm environment and the structures and evolutions of a tornadic storm in the vicinity of a triple point where three different air masses intersected over the irregular coastline of southern China were examined. Analysis was carried out primarily using X-PAR and S-Pol radar data, as well as surface weather station observations.

Compared to S-Pol, X-PAR presents more supercell-like features, such as mesocyclonic structures, notches, and hook echoes in its velocity and reflectivity products.

The tornadic storm occurred in a high-CAPE but low-shear environment when the South China Sea summer monsoon was active. Over the estuary of the Pearl River, surface cold outflows that were generated by pre-existing storms separately produced convergent boundaries with the southwesterly and southeasterly flows (Fig. 14a). The three types of air masses converged and contributed to an enhanced convergent zone over the boundary intersection point (or triple point). As a cold surge of westerly momentum at low levels approached this zone, finger-like pendant echoes formed (Fig. 14a). A subsequent reflectivity wrap-up process leading to hook echoes was identified over the triple point, indicating a strong low-to-middle level rotation in that region (Fig. 14b). The lowest TVS detected by X-PAR appeared shortly after a convective cell merged with the hook echoes.

The storm-boundary interaction under the influence of the monsoon, land–sea contrast, storm outflows, and the unique regional topography may be an important contribution to rotating storms (and even tornadoes) over the PRD. We have identified several tornadic storms that are similar to the current case in this region. While the observational analysis provides some insights into the role of the trumpet-shaped coastline in regard to the 1 June 2020 PRD tornadic event, a number of questions remain unanswered, such as the number of tornadoes that are associated with similar

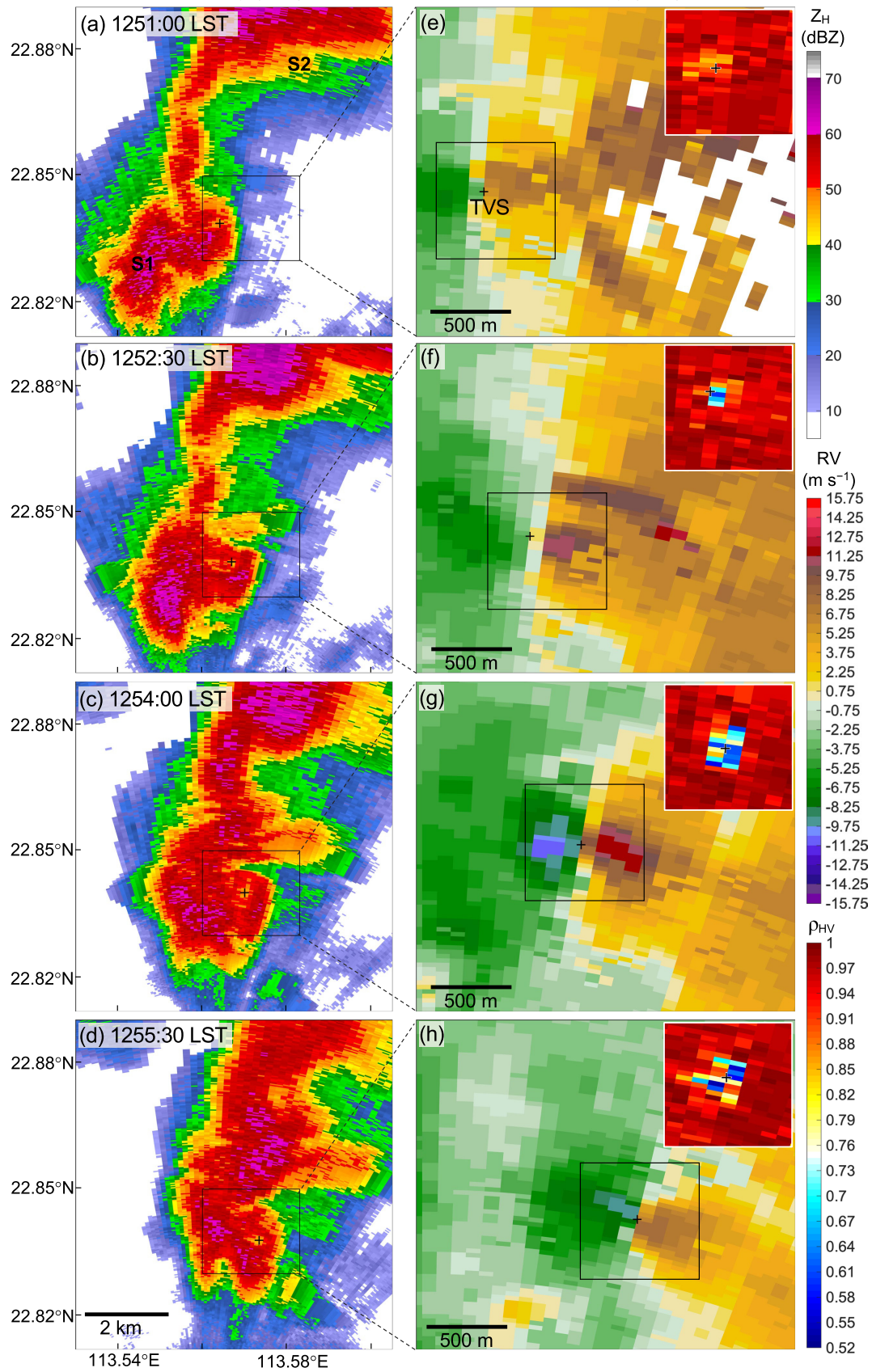


Fig. 12. (a–d) Reflectivity at the 0.9° elevation angle from X-PAR at different times on 1 June 2020. (e–h) The 0.9° radial velocity enlarged in the rectangular area around the hook echo. The centroid of TVS is marked by a cross. The copolar cross-correlation coefficient (ρ_{HV}) around the TVS (within the rectangle) is also shown in the upper-right corner.

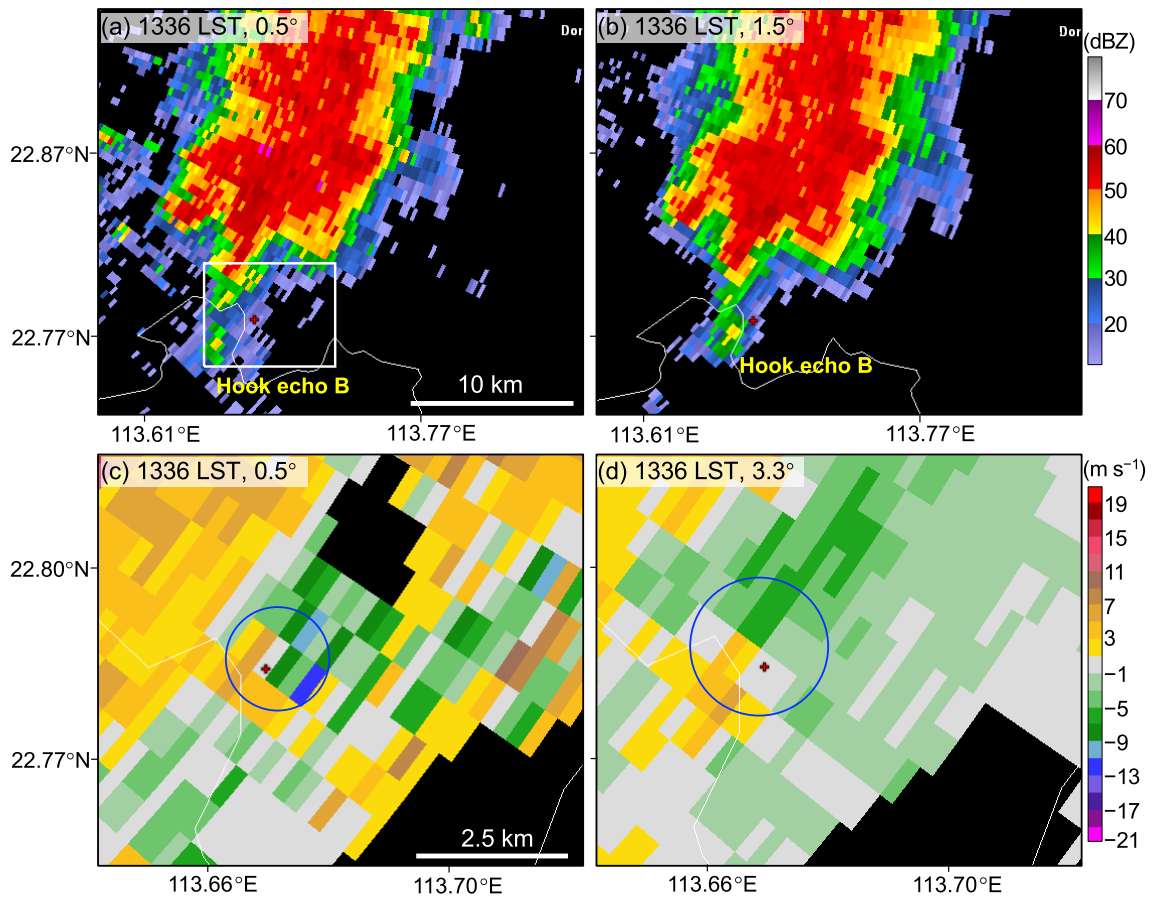


Fig. 13. (a, b) Radar reflectivity from S-pol valid at 1336 LST 1 June 2020. (c, d) Radial velocity around the hook echoes and the low-level mesovortex (blue circle) within the dashed box in (a). The red crosses are plotted for location reference.

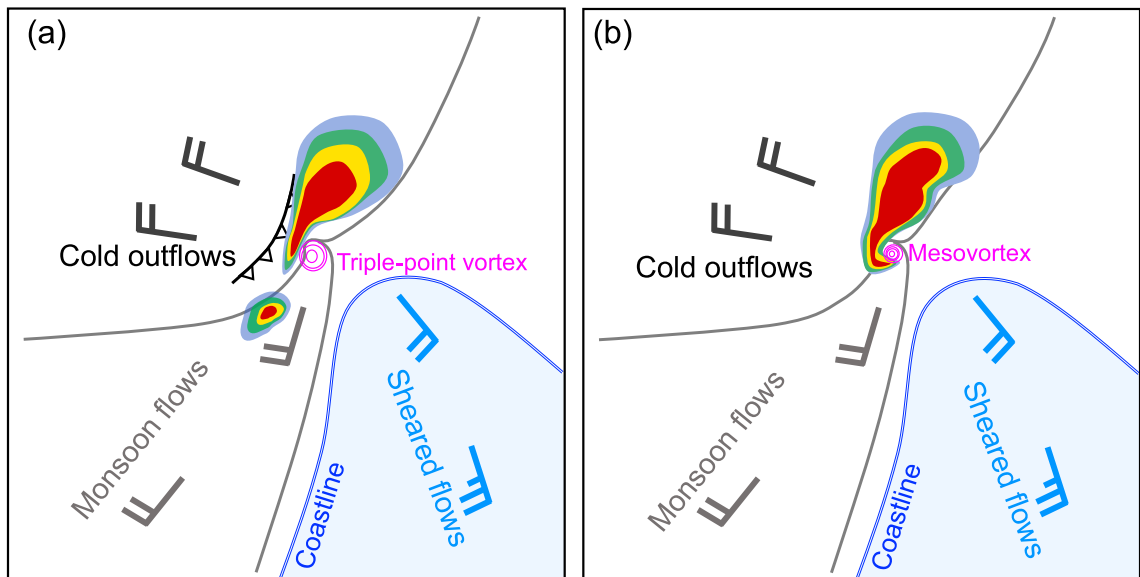


Fig. 14. Schematic of the mesovortex formation within a storm (shaded in multiple colors) occurring over the estuary of the PRD. Dashed curves represent the surface boundaries associated with the storm-generated cold outflows (black bars) and southwesterly (gray bars) and sheared (blue bars) monsoonal onshore flows. The enhanced vertical vorticity near the triple point is marked in magenta. The outflow boundary appears as a curve with triangles. The blue shading represents the PRD sea surface.

dynamics. The dependence of mesovortex predictability on the degree of representation of coastline fine structures in NWP models, especially in a low-shear environment, is also an interesting topic. As documented above, this study is novel in the sense that it documents a tornado event that is associated with the trumpet-shaped coastline. The unique land–sea contrast connects the severe weather and the regional climate, which may provide additional guidance for assessing tornado risk in this region. In the second paper (Part II) of this series, the results from a set of numerical simulations are analyzed to investigate the mesovortex genesis as discussed in the observational analysis.

Acknowledgements. This study was supported by the Guangdong Major Project of Basic and Applied Basic Research (Grant No. 2020B0301030004) and the National Natural Science Foundation of China (Grant Nos. 42275006 and 42030604), the Guangdong Basic and Applied Basic Research Foundation (Grant No. 2023A1515011705), and the Science and Technology Research Project for Society of Foshan (Grant No. 2120001008761). The reanalysis data used can be accessed at the ECMWF’s website (<https://cds.climate.copernicus.eu/cdsapp#!/dataset/reanalysis-era5-pressure-levels?tab=form>). The radar and surface observations were provided by the Guangzhou Meteorological Observatory. The authors are grateful for the helpful reviews provided by the editors and anonymous reviewers.

REFERENCES

- Anderson-Frey, A. K., Y. P. Richardson, A. R. Dean, R. L. Thompson, and B. T. Smith, 2019: Characteristics of tornado events and warnings in the southeastern United States. *Wea. Forecasting*, **34**, 1017–1034, <https://doi.org/10.1175/WAF-D-18-0211.1>.
- Atkins, N. T., K. M. Butler, K. R. Flynn, and R. M. Wakimoto, 2014: An integrated damage, visual, and radar analysis of the 2013 Moore, Oklahoma, EF5 Tornado. *Bull. Amer. Meteor. Soc.*, **95**, 1549–1561, <https://doi.org/10.1175/BAMS-D-14-00033.1>.
- Bai, L. Q., Z. Y. Meng, K. Sueki, G. X. Chen, and R. L. Zhou, 2020a: Climatology of tropical cyclone tornadoes in China from 2006 to 2018. *Science China Earth Sciences*, **63**, 37–51, <https://doi.org/10.1007/s11430-019-9391-1>.
- Bai, L. Q., G. X. Chen, and L. Huang, 2020b: Convection initiation in monsoon coastal areas (South China). *Geophys. Res. Lett.*, **47**, e2020GL087035, <https://doi.org/10.1029/2020GL087035>.
- Brady, R. H., and E. J. Szoke, 1989: A case study of nonmesocyclone tornado development in northeast Colorado: Similarities to waterspout formation. *Mon. Wea. Rev.*, **117**, 843–856, [https://doi.org/10.1175/1520-0493\(1989\)117<0843:ACSONT>2.0.CO;2](https://doi.org/10.1175/1520-0493(1989)117<0843:ACSONT>2.0.CO;2).
- Brooks, H. E., J. W. Lee, and J. P. Craven, 2003: The spatial distribution of severe thunderstorm and tornado environments from global reanalysis data. *Atmospheric Research*, **67–68**, 73–94, [https://doi.org/10.1016/S0169-8095\(03\)00045-0](https://doi.org/10.1016/S0169-8095(03)00045-0).
- Bunkers, M. J., B. A. Klimowski, J. W. Zeitler, R. L. Thompson, and M. L. Weisman, 2000: Predicting supercell motion using a new hodograph technique. *Wea. Forecasting*, **15**, 61–79, [https://doi.org/10.1175/1520-0434\(2000\)015<0061:PSMUAN>2.0.CO;2](https://doi.org/10.1175/1520-0434(2000)015<0061:PSMUAN>2.0.CO;2).
- Burgess, D., and Coauthors, 2014: 20 May 2013 Moore, Oklahoma, Tornado: Damage survey and analysis. *Wea. Forecasting*, **29**, 1229–1237, <https://doi.org/10.1175/WAF-D-14-00039.1>.
- Chen, X. C., F. Q. Zhang, and K. Zhao, 2016: Diurnal variations of the land–sea breeze and its related precipitation over South China. *J. Atmos. Sci.*, **73**, 4793–4815, <https://doi.org/10.1175/JAS-D-16-0106.1>.
- Davies-Jones, R., 1984: Streamwise vorticity: The origin of updraft rotation in supercell storms. *J. Atmos. Sci.*, **41**, 2991–3006, [https://doi.org/10.1175/1520-0469\(1984\)041<2991:SVTOOU>2.0.CO;2](https://doi.org/10.1175/1520-0469(1984)041<2991:SVTOOU>2.0.CO;2).
- Davies-Jones, R., 2006: Tornadogenesis in supercell storms: What we know and what we don’t know. *Preprints, Symp. on the Challenges of Severe Convective Storms*, Atlanta, GA, Amer. Meteor. Soc..
- Du, Y., and G. X. Chen, 2019a: Climatology of low-level jets and their impact on rainfall over Southern China during the early-summer rainy season. *J. Climate*, **32**, 8813–8833, <https://doi.org/10.1175/JCLI-D-19-0306.1>.
- Du, Y., and G. X. Chen, 2019b: Heavy rainfall associated with double low-level jets over Southern China. Part II: Convection initiation. *Mon. Wea. Rev.*, **147**, 543–565, <https://doi.org/10.1175/MWR-D-18-0102.1>.
- Fan, W. J., and X. D. Yu, 2015: Characteristics of spatial temporal distribution of tornadoes in China. *Meteorological Monthly*, **41**, 793–805, <https://doi.org/10.7519/j.issn.1000-0526.2015.07.001>.
- Fournoy, M. D., A. W. Lyza, M. A. Satrio, M. R. Diedrichsen, M. C. Coniglio, and S. Waugh, 2022: A climatology of cell mergers with supercells and their association with mesocyclone evolution. *Mon. Wea. Rev.*, **150**, 451–461, <https://doi.org/10.1175/MWR-D-21-0204.1>.
- Hersbach, H., and Coauthors, 2020: The ERA5 global reanalysis. *Quart. J. Roy. Meteor. Soc.*, **146**, 1999–2049, <https://doi.org/10.1002/qj.3803>.
- Hong, S. Y., and J. J. Lim, 2006: The WRF single-moment 6-class microphysics scheme (WSM6). *J. Korean Meteorological Soc.*, **42**(2), 129–151.
- Houston, A. L., and R. B. Wilhelmson, 2007a: Observational analysis of the 27 May 1997 central Texas Tornadic Event. Part I: Prestorm environment and storm maintenance/propagation. *Mon. Wea. Rev.*, **135**, 701–726, <https://doi.org/10.1175/MWR3300.1>.
- Houston, A. L., and R. B. Wilhelmson, 2007b: Observational analysis of the 27 May 1997 central Texas Tornadic Event. Part II: Tornadoes. *Mon. Wea. Rev.*, **135**, 727–735, <https://doi.org/10.1175/MWR3301.1>.
- Houston, A. L., and R. B. Wilhelmson, 2012: The impact of airmass boundaries on the propagation of deep convection: A modeling-based study in a high-CAPE, low-shear environment. *Mon. Wea. Rev.*, **140**, 167–183, <https://doi.org/10.1175/MWR-D-10-05033.1>.
- Kingsmill, D. E., 1995: Convection initiation associated with a sea-breeze front, a gust front, and their collision. *Mon. Wea. Rev.*, **123**, 2913–2933, [https://doi.org/10.1175/1520-0493\(1995\)123<2913:CIAWAS>2.0.CO;2](https://doi.org/10.1175/1520-0493(1995)123<2913:CIAWAS>2.0.CO;2).
- Lee, B. D., and R. B. Wilhelmson, 1997a: The numerical simulation of non-supercell tornadogenesis. Part I: Initiation and evolution of pretornadic mesocyclone circulations along a dry out-

- flow boundary. *J. Atmos. Sci.*, **54**, 32–60, [https://doi.org/10.1175/1520-0469\(1997\)054<0032:TNSONS>2.0.CO;2](https://doi.org/10.1175/1520-0469(1997)054<0032:TNSONS>2.0.CO;2).
- Lee, B. D., and R. B. Wilhelmson, 1997b: The numerical simulation of nonsupercell tornadogenesis. Part II: Evolution of a family of tornadoes along a weak outflow boundary. *J. Atmos. Sci.*, **54**, 2387–2415, [https://doi.org/10.1175/1520-0469\(1997\)054<2387:TNSONT>2.0.CO;2](https://doi.org/10.1175/1520-0469(1997)054<2387:TNSONT>2.0.CO;2).
- Lee, B. D., and R. B. Wilhelmson, 2000: The numerical simulation of nonsupercell tornadogenesis. Part III: Parameter tests investigating the role of CAPE, vortex sheet strength, and boundary layer vertical shear. *J. Atmos. Sci.*, **57**, 2246–2261, [https://doi.org/10.1175/1520-0469\(2000\)057<2246:TNSONT>2.0.CO;2](https://doi.org/10.1175/1520-0469(2000)057<2246:TNSONT>2.0.CO;2).
- Markowski, P., and Y. Richardson, 2010: *Mesoscale Meteorology in Midlatitudes*. Wiley-Blackwell, 407 pp.
- Marquis, J. N., Y. P. Richardson, and J. M. Wurman, 2007: Kinematic observations of mesocyclones along boundaries during IHOP. *Mon. Wea. Rev.*, **135**, 1749–1768, <https://doi.org/10.1175/MWR3367.1>.
- Mlawer, E. J., S. J. Taubman, P. D. Brown, M. J. Iacono, and S. A. Clough, 1997: Radiative transfer for inhomogeneous atmospheres: RRTM, a validated correlated-k model for the longwave. *J. Geophys. Res.: Atmos.*, **102**, 16 663–16 682, <https://doi.org/10.1029/97JD00237>.
- Noh, Y., W. G. Cheon, S. Y. Hong, and S. Raasch, 2003: Improvement of the K-profile model for the planetary boundary layer based on large eddy simulation data. *Bound.-Layer Meteor.*, **107**, 401–427, <https://doi.org/10.1023/A:1022146015946>.
- Orlanski, I., 1975: A rational subdivision of scales for atmospheric processes. *Bull. Amer. Meteor. Soc.*, **56**, 527–530, <https://doi.org/10.1175/1520-0477-56.5.527>.
- Reed, R. J., and M. D. Albright, 1997: Frontal structure in the interior of an intense mature ocean cyclone. *Wea. Forecasting*, **12**, 866–876, [https://doi.org/10.1175/1520-0434\(1997\)012<0866:FSITIO>2.0.CO;2](https://doi.org/10.1175/1520-0434(1997)012<0866:FSITIO>2.0.CO;2).
- Rotunno, R., 1981: On the evolution of thunderstorm rotation. *Mon. Wea. Rev.*, **109**, 577–586, [https://doi.org/10.1175/1520-0493\(1981\)109<0577:OTEOTR>2.0.CO;2](https://doi.org/10.1175/1520-0493(1981)109<0577:OTEOTR>2.0.CO;2).
- Rotunno, R., and J. Klemp, 1985: On the rotation and propagation of simulated supercell thunderstorms. *J. Atmos. Sci.*, **42**, 271–292, [https://doi.org/10.1175/1520-0469\(1985\)042<0271:OTRAPO>2.0.CO;2](https://doi.org/10.1175/1520-0469(1985)042<0271:OTRAPO>2.0.CO;2).
- Schenkman, A. D., M. Xue, and A. Shapiro, 2012: Tornadogenesis in a simulated mesovortex within a mesoscale convective system. *J. Atmos. Sci.*, **69**, 3372–3390, <https://doi.org/10.1175/JAS-D-12-038.1>.
- Schumacher, R. S., 2015: Resolution dependence of initiation and upscale growth of deep convection in convection-allowing forecasts of the 31 May–1 June 2013 supercell and MCS. *Mon. Wea. Rev.*, **143**, 4331–4354, <https://doi.org/10.1175/MWR-D-15-0179.1>.
- Skamarock, W. C., and Coauthors, 2008: A description of the Advanced Research WRF version 3. NCAR Tech. Note NCAR/TN-475+STR, 113 pp.
- Thompson, R. L., B. T. Smith, A. R. Dean, and P. T. Marsh, 2013: Spatial distributions of tornadic near-storm environments by convective mode. *E-Journal of Severe Storms Meteorology*, **8**, 1–22, <https://doi.org/10.55599/ejssm.v8i5.50>.
- Thompson, R. L., R. Edwards, J. A. Hart, K. L. Elmore, and P. Markowski, 2003: Close proximity soundings within supercell environments obtained from the rapid update cycle. *Wea. Forecasting*, **18**, 1243–1261, [https://doi.org/10.1175/1520-0434\(2003\)018<1243:CPSWSE>2.0.CO;2](https://doi.org/10.1175/1520-0434(2003)018<1243:CPSWSE>2.0.CO;2).
- Thompson, R. L., B. T. Smith, J. S. Grams, A. R. Dean, and C. Broyles, 2012: Convective modes for significant severe thunderstorms in the contiguous United States. Part II: Supercell and QLCS tornado environments. *Wea. Forecasting*, **27**, 1136–1154, <https://doi.org/10.1175/WAF-D-11-00116.1>.
- Wakimoto, R. M., and J. W. Wilson, 1989: Non-supercell Tornadoes. *Mon. Wea. Rev.*, **117**, 1113–1140, [https://doi.org/10.1175/1520-0493\(1989\)117<1113:NST>2.0.CO;2](https://doi.org/10.1175/1520-0493(1989)117<1113:NST>2.0.CO;2).
- Wakimoto, R. M., H. V. Murphey, E. V. Browell, and S. Ismail, 2006: The “Triple Point” on 24 May 2002 during IHOP. Part I: Airborne Doppler and LASE analyses of the frontal boundaries and convection initiation. *Mon. Wea. Rev.*, **134**, 231–250, <https://doi.org/10.1175/MWR3066.1>.
- Wang, B., and LinHo, 2002: Rainy season of the Asian–Pacific summer monsoon. *J. Climate*, **15**, 386–398, [https://doi.org/10.1175/1520-0442\(2002\)015<0386:RSOTAP>2.0.CO;2](https://doi.org/10.1175/1520-0442(2002)015<0386:RSOTAP>2.0.CO;2).
- Weckwerth, T. M., and D. B. Parsons, 2006: A review of convection initiation and motivation for IHOP_2002. *Mon. Wea. Rev.*, **134**, 5–22, <https://doi.org/10.1175/MWR3067.1>.
- Weiss, C. C., and H. B. Bluestein, 2002: Airborne pseudo-dual Doppler analysis of a dryline-outflow boundary intersection. *Mon. Wea. Rev.*, **130**, 1207–1226, [https://doi.org/10.1175/1520-0493\(2002\)130<1207:APDDAO>2.0.CO;2](https://doi.org/10.1175/1520-0493(2002)130<1207:APDDAO>2.0.CO;2).
- Wurman, J., K. Kosiba, P. Robinson, and T. Marshall, 2014: The role of multiple-vortex tornado structure in causing storm researcher fatalities. *Bull. Amer. Meteor. Soc.*, **95**, 31–45, <https://doi.org/10.1175/BAMS-D-13-00221.1>.
- Wurman, J., J. Straka, E. Rasmussen, M. Randall, and A. Zahrai, 1997: Design and deployment of a portable, pencil-beam, pulsed, 3-cm Doppler radar. *J. Atmos. Oceanic Technol.*, **14**, 1502–1512, [https://doi.org/10.1175/1520-0426\(1997\)014<1502:DADOAP>2.0.CO;2](https://doi.org/10.1175/1520-0426(1997)014<1502:DADOAP>2.0.CO;2).
- Xue, M., and W. J. Martin, 2006a: A high-resolution modeling study of the 24 May 2002 dryline case during IHOP. Part I: Numerical simulation and general evolution of the dryline and convection. *Mon. Wea. Rev.*, **134**, 149–171, <https://doi.org/10.1175/MWR3071.1>.
- Xue, M., and W. J. Martin, 2006b: A high-resolution modeling study of the 24 May 2002 dryline case during IHOP. Part II: Horizontal convective rolls and convective initiation. *Mon. Wea. Rev.*, **134**, 172–191, <https://doi.org/10.1175/MWR3072.1>.
- Zhang, Q. H., X. Ni, and F. Q. Zhang, 2017: Decreasing trend in severe weather occurrence over China during the past 50 years. *Scientific Reports*, **7**, 42310, <https://doi.org/10.1038/srep42310>.
- Zhang, Y., L. Q. Bai, Z. Y. Meng, B. H. Chen, C. C. Tian, and P. L. Fu, 2021: Rapid-scan and polarimetric phased-array radar observations of a tornado in the Pearl River Estuary. *Journal of Tropical Meteorology*, **27**, 81–86, <https://doi.org/10.46267/j.1006-8775.2021.008>.
- Zhang, Y. J., F. Q. Zhang, D. J. Stensrud, and Z. Y. Meng, 2015: Practical predictability of the 20 May 2013 Tornadic thunderstorm event in Oklahoma: Sensitivity to synoptic timing and topographical influence. *Mon. Wea. Rev.*, **143**, 2973–2997, <https://doi.org/10.1175/MWR-D-14-00394.1>.
- Zhou, R. L., Z. Y. Meng, and L. Q. Bai, 2022: Differences in tornado activities and key tornadic environments between China and the United States. *International Journal of Climatology*, **42**, 367–384, <https://doi.org/10.1002/joc.7248>.